

LetsGo: Large-Scale Garage Modeling and Rendering via LiDAR-Assisted Gaussian Primitives

Jiadi Cui^{1,4*}, Junming Cao^{3,6*}, Fuqiang Zhao^{1,5*}, Zhipeng He¹, Yifan Chen¹, Yuhui Zhong², Lan Xu¹,
 Yujiao Shi¹, Yingliang Zhang^{2†}, and Jingyi Yu^{1†}

¹ShanghaiTech University, ²DGene, ³Shanghai Advanced Research Institute, CAS, ⁴Stereeye, ⁵NeuDim

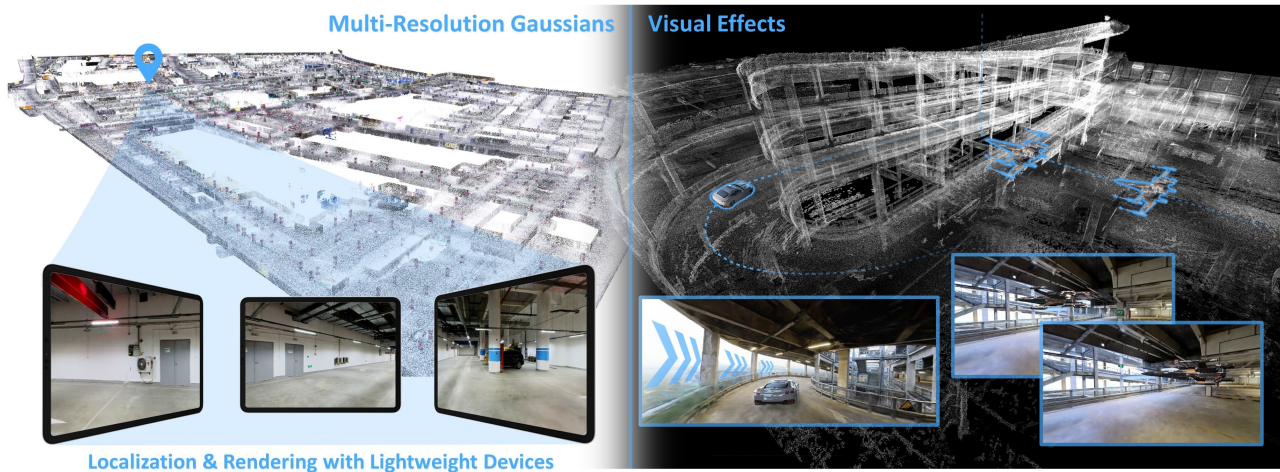


Figure 1: We present LetsGo - an explicit and efficient end-to-end framework for high-fidelity rendering of large-scale garages. We design a handheld Polar scanner to capture RGBD data of expansive parking environments and have scanned a garage dataset, named GarageWorld, comprising eight garages with different structures. Our LiDAR-assisted Gaussian primitives approach along with GarageWorld dataset enables various applications, such as autonomous vehicle localization, navigation and parking, as well as VFX production.

Abstract

Large garages are ubiquitous yet intricate scenes that present unique challenges due to their monotonous colors, repetitive patterns, reflective surfaces, and transparent vehicle glass. Conventional Structure from Motion (SfM) methods for camera pose estimation and 3D reconstruction often fail in these environments due to poor correspondence construction. To address these challenges, we introduce LetsGo, a LiDAR-assisted Gaussian splatting framework for large-scale garage modeling and rendering. We develop a handheld scanner, Polar, equipped with IMU, Li-

DAR, and a fisheye camera, to facilitate accurate data acquisition. Using this Polar device, we present the GarageWorld dataset, consisting of eight expansive garage scenes with diverse geometric structures, which will be made publicly available for further research. Our approach demonstrates that LiDAR point clouds collected by the Polar device significantly enhance a suite of 3D Gaussian splatting algorithms for garage scene modeling and rendering. We introduce a novel depth regularizer that effectively eliminates floating artifacts in rendered images. Additionally, we propose a multi-resolution 3D Gaussian representation designed for Level-of-Detail (LOD) rendering. This includes adapted scaling factors for individual levels and a random-resolution-level training scheme to optimize the Gaussians across different resolutions. This representa-

* Authors contributed equally to this work.

† These authors are corresponding authors.

tion enables efficient rendering of large-scale garage scenes on lightweight devices via a web-based renderer. Experimental results on our GarageWorld dataset, as well as on ScanNet++ and KITTI-360, demonstrate the superiority of our method in terms of rendering quality and resource efficiency.

1. Introduction

Modeling garage environments accurately is crucial for various applications such as autonomous vehicle testing, architectural planning, and game design. Garages present a unique set of challenges due to their complex geometries, varying lighting conditions, and frequent presence of obstacles. The ability to create detailed and realistic 3D models of garages can significantly enhance the effectiveness of these applications, providing more accurate simulations and analyses. For visual artists, garages represent a frontier in visual simulation that merges the aesthetic with the technical, offering a canvas where the intricacies of light, shadow, texture, and space coalesce. The complex interplay of artificial and natural lighting within the confines of a garage, with its reflective surfaces, varying materials, and intricate geometries, provides a rigorous testbed for modeling and rendering, pushing the boundaries of what is achievable in virtual environments.

However, capturing and rendering garage environments pose significant difficulties. These spaces often have low-light conditions, textureless surfaces, and a high degree of clutter (Fig.5). The intricacies of garage layouts, including narrow spaces and reflective surfaces, further complicate the modeling process. Garages with internal circular or spiral paths often lead to incomplete data and ambiguities in spatial relationships. Additionally, their extensive spatial area underscores the necessity for efficient 3D representations and lightweight rendering techniques to facilitate real-time interaction and visualization, particularly for scenarios demanding rapid situational assessment, such as navigation and path adjustment.

Existing methods for garage modeling typically rely on either manual measurements or conventional photogrammetry and LiDAR scanning. Traditional computer vision techniques, such as Structure from Motion (SfM)[71, 65] and Multi-view Stereo (MVS[91, 24]), often struggle in these environments due to the prevalence of texture-less regions and repetitive structural designs. These methods frequently fail to extract sufficient feature points and establish accurate feature correspondences necessary for estimating camera poses. Active sensing technologies based on LiDAR can calculate camera poses and scene geometry using SLAM algorithms, but the reflective materials and transparent car windows common in garages lead to geometric inaccuracies. Moreover, LiDAR data tend to be sparse, con-

taining many holes that corrupt high-frequency textures essential for rendering the color appearance of the scene.

While recent advances in neural representation, particularly Neural Radiance Fields (NeRF)[51], have shown promise in producing high-quality renderings, they come with high computational costs and lengthy training times. Although enhancements [72, 95, 88, 16] to NeRF aim to optimize training duration and visual rendering quality, integrating such implicit representations into conventional graphics rendering pipelines and tools for rapid 3D content applications remains challenging. The emerging 3D Gaussian Splatting (3DGS)[34] method revisits explicit representations, using 3D Gaussians to articulate the geometry and appearance of scenes, achieving high-quality scene modeling and rendering. Recent works [35, 47, 61, 48, 70] extend the 3DGS approach to model large-scale outdoor scenes, achieving impressive results. However, few methods address the unique challenges of modeling large-scale indoor scenes like underground garages, where low lighting, large texture-less regions, and repetitive patterns complicate the establishment of sufficient feature correspondences between different images.

This paper introduces LetsGo, an explicit and efficient end-to-end modeling scheme for high-fidelity rendering of large-scale garages. Our key innovation is the integration of calibrated LiDAR points into 3D Gaussian splatting algorithms. We design a handheld Polar scanner, which combines IMU, LiDAR, and a fisheye camera for robust relative pose estimation, specifically tailored for expansive garage data collection. We scan eight large-scale garages, collectively named GarageWorld, using this Polar scanner. To our knowledge, this dataset is the first of its kind aimed at large-scale garages and will be made available to the community. Our experiments demonstrate that LiDAR points collected by the Polar device effectively support various Gaussian splatting algorithms for detailed garage scene representation. To enhance the quality of 3D Gaussian rendering, we introduce a depth regularizer that uses depth priors as supervisory signals, significantly reducing floating artifacts and enabling high rendering quality.

As the scene size increases, the memory demands for rendering large amounts of 3D Gaussians can exceed the capabilities of even high-end GPUs. To address this challenge, we propose a multi-resolution 3D Gaussian representation tailored for Level-of-Detail (LOD) rendering. This approach dynamically adjusts based on the camera’s position, orientation, and viewing frustum, allowing for real-time, high-quality rendering of expansive scenes. Specifically, we construct different levels of Gaussians at varying resolutions, where lower-resolution levels capture coarse scene characteristics and higher-resolution levels reconstruct fine, high-frequency details. We employ tailored scaling factors for each level and a random-resolution-level

training scheme to optimize the Gaussians across different levels.

During rendering, we introduce a novel level selection strategy that optimizes the trade-off between visual fidelity and device performance by considering the distance between 3D Gaussians and the rendering viewpoint. With our multi-resolution 3D Gaussian framework, we develop an LOD PC viewer that achieves rendering speeds up to four times faster than traditional 3DGS viewers on high-performance GPUs (*e.g.*, RTX 3090). Additionally, we offer a lightweight web renderer designed to support LOD rendering across various consumer-level devices, including laptops and tablets. We will release our source codes, including our training code, high-performance PC viewer, and lightweight web viewer, to facilitate reproducible research.

Our results, gathered from the GarageWorld dataset as well as ScanNet++[13] and KITTI-360[44] datasets, indicate that our approach not only surpasses other methods in rendering quality but also maintains high rendering efficiency. The GarageWorld dataset and the LetsGo framework for large-scale garage modeling and rendering enable various applications, including autonomous driving, localization, navigation, visual effects, *etc.*

2. Related Work

Conventional Explicit Visual Reconstruction. Conventional algorithms for reconstructing large-scale scenes include Structure from Motion (SfM) [82, 74, 52], Simultaneous Localization and Mapping (SLAM) [40, 4, 5, 6] and Multi-View Stereo (MVS) [68, 25, 23]. They are dedicated to discerning the three-dimensional structure of a scene through the sequential or multi-view analysis of two-dimensional image frames. All these methods leverage feature tracking and multi-view consistency to recover the 3D scene structures. SfM- and SLAM-based methods [12, 1, 19, 28, 78, 64, 42] estimate poses of input images and recover the scene structure jointly. However, their main purpose is pose estimation, and the recovered scene point clouds are always sparse, making it difficult for high-quality free-view synthesis. While MVS-based methods [41, 15, 29, 90, 87, 86], especially deep-based approaches, compute a dense depth map for each input image, the constructed scenes often lack accuracy and robustness in texture-less and complex scenes.

NeRF and 3D Gaussian Splatting Variants. Recent advances [55, 9, 93, 36, 58, 98, 97] in neural scene representation have significantly impacted novel view synthesis. Neural Radiance Fields (NeRF), introduced by Mildenhall et al. [51], have revolutionized 3D reconstruction with a novel framework for detailed scene capture. Subsequent improvements [73, 38, 62, 60] have aimed at enhancing the visual fidelity and computational efficiency of NeRF. MipNeRF [2]

and MipNeRF360 [3] address aliasing via a novel conical frustum rendering technique and a nonlinear scene representation, respectively. Techniques such as Plexnoxels [20], Instant-NGP [53], and TensorRF [8] have expedited rendering by integrating explicit encoding methods with compact MLP networks. Furthermore, Block-NeRF [75] and Mega-NeRF [79] facilitate the application of NeRF to extensive scenes. F2-NeRF [81] introduces a space-warping method for handling arbitrary camera trajectories. ScaNeRF [84] optimizes camera pose and scene representation jointly to address pose drift in large-scale scene reconstruction. Unlike these NeRF-based approaches, our method employs an explicit 3D Gaussian representation with depth priors from our RGBD scanner, enhancing realism and efficiency.

3D Gaussian Splatting (3DGS)[34] is a transformative approach characterized by its efficiency and lifelike visual quality. Extensive research [48, 54, 33, 49, 7, 83, 31, 77] has built on 3DGS. Mip-Splatting [94] mitigates artifacts from varying view sampling rates, and GaussianPro [10], which enhances Gaussian distribution with 2D image constraints. DN-Splatter [80] and DNGaussian [43] use depth and normal cues for refinement. SuGaR [27] introduces Gaussian alignment regularization for explicit mesh extraction, and GaussianSurfels [14] flattens 3D Gaussian ellipsoids into 2D ellipses for accurate surface reconstructions. 2DGS [30] transforms 3D volumes into 2D planar Gaussian disks, employing a perspective-accurate 2D splatting process aligned with geometric surfaces. Despite these advances focusing on small-scale or object-level scenes, our approach innovates with a depth regularizer and a multi-resolution Gaussian representation designed for large-scale scenes, achieving realistic visual quality and enhanced rendering efficiency.

Gaussian Splatting for Large-Scale Scenes. To effectively manage large-scale scenes, VastGaussian [46] explores various partitioning strategies and introduces an appearance embedding module to enhance Gaussian training. Concurrent works such as DrivingGaussian [99] and Street Gaussian [89] adapt Gaussian methodologies to the dynamic contexts of urban landscapes and autonomous driving scenarios, respectively. In addition, multiple studies are integrating the Level of Detail (LOD) rendering technique with 3D Gaussian Splatting to balance rendering quality and speed. Traditional mesh-based LOD strategies [57, 11] create varying levels of detail in object meshes, selecting the appropriate level based on the viewer’s distance to the target or the desired quality. Point-based LOD methods, like Potree [66] and FastLOD [67], are designed to efficiently render large 3D point clouds, which is particularly beneficial for LiDAR data visualization.

Recently, Octree-GS [61] proposes representing Gaussians within an octree structure to render fine details at dif-

ferent viewing scales. CityGaussian [47] employs an LOD strategy for efficiently training and rendering of large-scale 3DGS. Hierarchical 3DGS [35] introduces a hierarchical 3DGS, showing promising results in rendering extensive walk-through datasets. However, these methods lack of on-demand rendering schemes and require high-computational devices to load complete scenes for real-time rendering, making them unsuitable for lightweight devices such as tablets or laptops. In contrast, our LetsGo method employs a multi-resolution Gaussian representation coupled with an on-demand rendering scheme. This approach achieves rendering speeds four times faster than the original 3DGS and ensures compatibility with lightweight devices, facilitating real-time rendering in large-scale garage scenes.

3. Garage Data Capture

3.1. Raw Data Acquisition

Scanning and modeling a large garage is a non-trivial task. Underground and indoor garages often face challenges in receiving GPS signals due to the physical barriers presented by the structures and materials surrounding them, making camera pose estimation for scanning and modeling difficult. Furthermore, there are always large-scale textureless regions inside a garage, *e.g.*, floors and walls. The parked vehicles often contain transparent glasses, and their surfaces are sometimes reflective. This complicates feature matching between images for camera pose estimation and 3D geometry reconstruction. Using a LiDAR sensor for scanning and modeling can provide detailed geometric information. However, the RGB color for each scanned point is not associated.

Capturing Device. To address these problems, we design a lightweight handheld scanning device named “Polar” to jointly collect color and geometric information of the garage. The data collection unit of the Polar device comprises a color fisheye camera, a LiDAR sensor, and an IMU sensor, as visualized in Fig. 2. The fisheye camera captures RGB color information in 30 FPS. It has a resolution of 6K and a field of view (FOV) of 180×180 degrees, allowing for quick and comprehensive recording of vivid color data. The LiDAR sensor collects 3D point clouds, recording geometric information at a rate of 2.6 million points per second. With a measurement accuracy of 1 to 1.5 cm and a maximum detection distance of 50 m, it is ideal for 3D scanning of large garage scenes. The IMU sensor provides acceleration information on the device’s motion, enabling more accurate pose estimation. In addition to the data acquisition unit, we also equip the Polar device with a data processing unit consisting of a mini PC for real-time SLAM calculations. The data processing unit is powered by two removable batteries that provide more than 30 minutes of single scan endurance. With this unit, one can use a smartphone to

connect with the Polar device and preview 3D point cloud reconstruction results in real-time. More information about Polar device along with the calibration process is provided in Appendix.A.

Scanning Scheme. We use the Polar device to scan various garages for modeling and free-viewpoint rendering. The scanning trajectory for each garage is meticulously designed to emulate drive-through and parking. We collect data along each trajectory four times: one for forward-facing, one for backward-facing, one for side-left, and one for side-right, ensuring comprehensive capturing of the garage. We set the camera to auto exposure and auto ISO to accommodate complex lighting changes in the garage. For garages that are partially open-air and partially covered, the data is collected when the sunlight is weak, *i.e.*, during the early morning or evening. This ensures the images captured in the transition between open-air and covered areas share similar illumination. We also apply a short pause for data capturing at the transition area, allowing the sensor to adapt to different lighting conditions and thus ensuring the images are neither overexposed nor underexposed. For garages with motion-activated lights, we ensure the data is collected after the light turns on, maintaining consistent lighting conditions across all images. The travel speed for data collection is at around 1.0 ± 0.2 m/s, with a turning speed of $15^\circ \pm 3$ °/s. To avoid motion blur in areas with insufficient light, these parameters are reduced to 0.5 m/s and 10 °/s, respectively. Some garages are very large, for example, over 30,000 square meters. Thus, we divide the large garage into small subsections and collect data for each subsection. The data is fused later after collection.

3.2. GarageWorld Dataset

We collect data for eight garages[†], including six underground garages with various types of inside geometries, one indoor garage with multi-floors at Shopping Mall One, and one outdoor surface parking at Shopping Mall Two. We plan to share the datasets with the community for further research. These garages comprise various challenging structures, such as sloped surfaces with distorted lines, internal circular or spiral paths, vehicle elevators, *etc.*, as shown in Fig. 5. Tab. 1 provides an overall description of the garages.

Underground Garages. Most of our captured garages are located underground. This architectural choice is prevalent in regions where above-ground space is scarce, allowing the conservation of surface area for alternative applications. Our underground garages on campus feature a single parking level, characterized by flat and sloped surfaces, and are lit by regular fluorescent light tubes affixed to the ceilings. In contrast, the garages at Shopping Mall Three and the Arts Center have vibrant design elements and superior lighting conditions. Additionally, we conduct a scan of a

[†]All garage data is captured with the necessary permits.

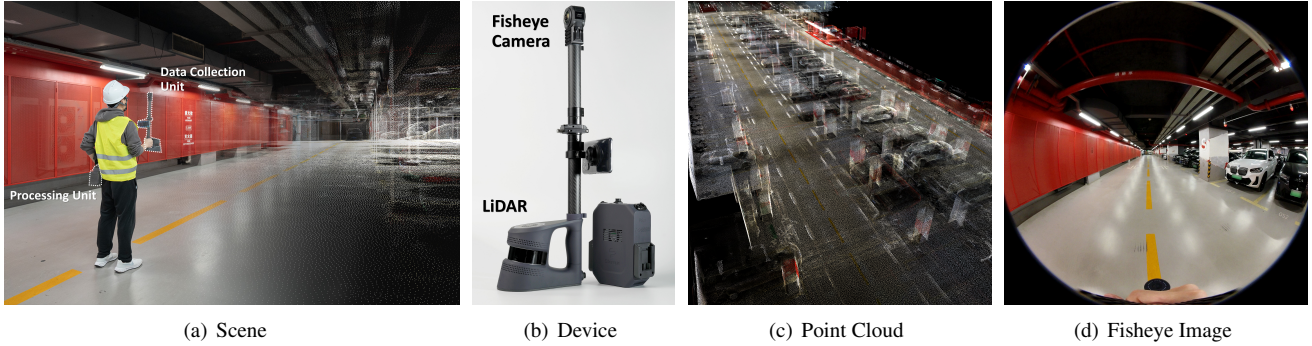


Figure 2: Our compact Polar scanner (b) is engineered for capturing expansive garage environments (a). It is optimized for handheld operation or vehicular mounting, enabling versatile data capture in extensive spaces. At the core of Polar’s data acquisition unit lies a high-fidelity LiDAR sensor, capturing precise 3D point clouds (c), complemented by a fisheye camera that procures wide-angle 2D RGB images (d) for a complete scene modeling.

Table 1: Detailed illustrations of our GarageWorld dataset, including various datasets categorized by their environment type, geometric features, area size, number of images, point count, face count, and lighting conditions

Dataset	Category	Geometry	Aera(m^2)	Image Num	Point Num	Face Num	Lighting Condition
Campus 1	Underground	Flat & Sloped Paths	38447.86	8479	1.9B	121.9M	Uniform Lighting
Campus 2	Underground	Flat & Sloped Paths	28046.37	7772	1.4B	95.8M	Uniform Lighting
Shopping Mall 1	Indoor (Multi-floors)	Spiral & Circular Paths	32646.68	5792	1.14B	40.8M	Uneven Lighting
Shopping Mall 2	Outdoor	Spiral & Sloped Paths	13495.92	2280	0.6B	77.1M	Natural Lighting
Shopping Mall 3	Underground	Flat & Sloped Paths	30246.07	13296	1.6B	106.1M	Uniform Lighting
Office Building	Underground	With Mechanical Parking System	22159.25	9308	1.15B	72.3M	Motion Sensor Lighting
Arts Center	Underground	Flat & Sloped Paths	10392.32	5779	0.52B	31.4M	Uniform Lighting
Subway Garage	Underground	Flat & Sloped Paths	7109.12	3607	0.70B	43.5M	Uniform Lighting

compact indoor garage within an office building, equipped with a mechanical parking system and featuring colored surfaces.

Indoor Garage with Multi-floor. Staking garages to multi-floor is a common design in dense urban environments. We collect data for this type of parking garage in Shopping Mall One. The different floors of this garage are connected by spiral and circular paths, which have a semi-open structure and are partially illuminated by sunlight and partially by indoor lights. Given that the lights in the shopping mall are not turned on in the early morning, we collect data for this garage during the early evening to maintain consistent illumination between different images.

Outdoor Parking. The outdoor surface parking facility is often in areas with large spaces or on the top of a commercial building. We collect data for a garage with this type located on the top of Shopping Mall Two. The entrance to this parking space is from indoor to outdoor, containing spiral and sloped paths. During daylight time, the outdoor illumination is stronger than indoor. At night, the limited dim streetlights are insufficient for photography requirements. Therefore, we conduct our data capture during the early morning and evening when the sunlight is soft, and the illumination between indoors and outdoors is similar.

3.3. Initial Mesh Reconstruction

We employ the off-the-shell LiDAR-Inertial-Visual(LIV) SLAM [69] to estimate the relative poses of the sensor between different time steps. The LIV-SLAM system integrates a tightly coupled LiDAR-Inertial Odometry and Visual-Inertial Odometry, along with a joint optimization approach between LiDAR and camera data, for relative pose estimation. The pose estimation system leverages the unique capabilities of each sensor of our Polar device to enhance overall accuracy and robustness. The IMU delivers reliable short-term motion estimates, while the LiDAR contributes precise distance measurements. Visual sensors complement these by enriching pose estimation in environments abundant with visual features, ensuring a robust and precise outcome.

After merging the point cloud data collected at different time steps using the estimated relative pose, we apply Poisson Reconstruction [32] to convert the point cloud data into a mesh. To ensure the accuracy and integrity of the resulting mesh, we also compare the reconstructed mesh to the original point cloud data to remove incorrect faces (More details in Appendix.B). This geometry-based mesh reconstruction method performs well for Lambertian surface reconstruction. However, it faces challenges for reflective and transparent surfaces, *e.g.*, vehicle glass windows, which is

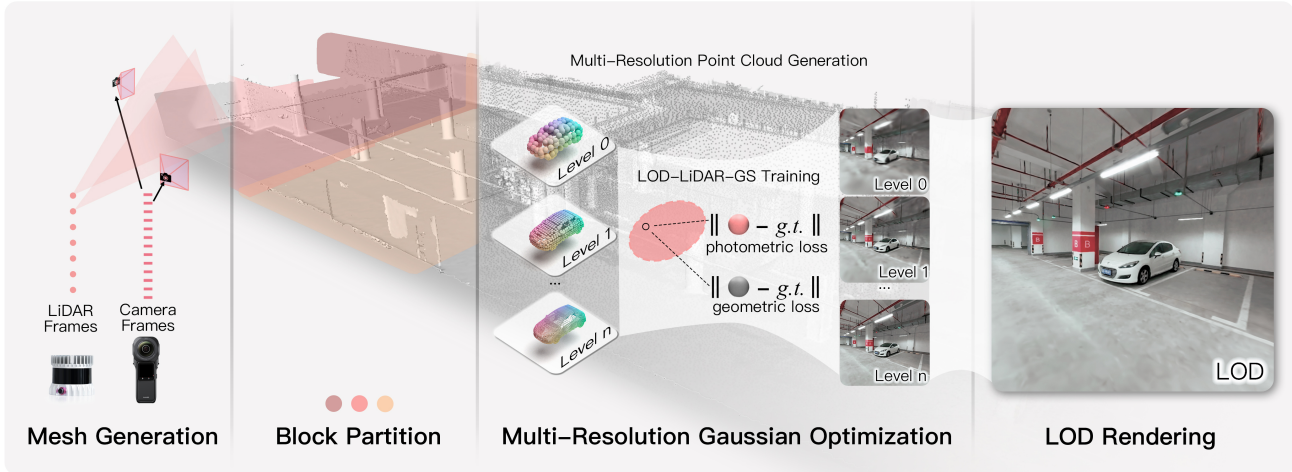


Figure 3: Overview of our LiDAR-assisted Gaussian splatting framework. Initially, we generate a base mesh using color and depth data collected by our self-designed Polar device. The data is then partitioned into blocks for parallel and rapid processing. Next, we downsample the high-quality scanned point clouds into multi-resolution point cloud for our LOD-LiDAR-RGS (Sec.4.2) method initialization. In addition to photometric supervision, we apply our novel unbiased Gaussian depth regularizer (Sec.4.1) for geometric supervision. Finally, our system produces photorealistic LOD rendering results based on the optimized multi-resolution Gaussian representation.

especially common in garage environments.

4. LiDAR-Assisted LoD Gaussian

3D Gaussian representation excels at modeling transparent and reflective surfaces compared to mesh. However, it requires a sparse 3D point cloud of the scene and accurate camera parameters obtained from SfM. As discussed previously, the large-scale garage scenes are challenging for SfM algorithms, with low lighting conditions, large textureless regions, repetitive patterns, *etc.*, making sufficient feature correspondences between different images hard to establish. As a result, the capacity of the original 3DGS for high-quality modeling and rendering is limited.

Our Polar scanner, equipped with calibrated IMU, LiDAR, and fisheye camera sensors, effectively addresses this challenge. By integrating the unique strengths of these diverse sensors, our system achieves precise camera localization and detailed 3D point cloud generation. In the following sections, we first delve into the technical details of our novel LiDAR-assisted Gaussian splatting technique (Sec. 4.1), which incorporates a custom depth regularizer. By leveraging geometry priors derived from our RGBD scans, this method enhances the realism of rendered images and minimizes the occurrence of floater artifacts. Subsequently, we introduce an innovative framework incorporating Level-of-Detail (LOD) technology into our Gaussian training and rendering process (Sec. 4.2). This framework utilizes a multi-resolution point cloud as its input, significantly boosting rendering speeds. Moreover, we show how it can facilitate rendering expansive garage environments on

lightweight devices through a specialized web-based renderer (Sec. 4.3). Fig.3 provides an overview of our LiDAR-assisted Gaussian splatting framework.

4.1. Gaussian Splatting with LiDAR Inputs

3DGS [34] represents 3D points with 3D Gaussians, parameterized by position μ , opacity α , anisotropic covariance Σ , and spherical harmonic (SH) coefficients representing view-dependent color c . The projection from 3D Gaussians to 2D images [101] is given by

$$\Sigma' = JW\Sigma W^T J^T, \quad (1)$$

where J represents the Jacobian of the affine approximation of the projective transformation, and W corresponds to the viewing transformation.

The purpose is to optimize the Gaussian parameters so that the rendered images from the 3D Gaussians are as close to their ground truth (GT) images as possible. Normally, the optimization is achieved by stochastic gradient descent (SGD). Since it cannot constrain the covariance matrix to be semi-definite, only in which scenario the covariance matrix has its physical meaning, Kerbl *et al.* proposes to optimize a scaling matrix S and rotation matrix R , and compute the covariance matrix as:

$$\Sigma = RSS^T R^T, \quad (2)$$

where S is parameterized as a 3D vector and R is parameterized as quaternion, a 4D vector with an unit norm.

Since conventional SfM approaches fail in large garage environments due to hard correspondence establishment between textureless and transparent regions, we use our Polar device with a LiDAR sensor to scan point clouds of the garages. Considering the originally scanned point clouds contain noises, we resample a set of new points from the reconstructed mesh with a uniform sampling strategy. These resampled points, in conjunction with the camera parameters, are used to train the 3DGS representations.

In addition to the image reconstruction loss in the original Gaussian splatting, we further introduce a depth-regularizer for our LiDAR-assisted 3DGS training, which incorporates depth priors derived from the high-quality LiDAR data during training. We denote this method as LiDAR-GS and the original 3DGS method with LiDAR-assisted point cloud for Gaussian initialization as 3DGS*.

Depth Regularizer. Inspired by the depth calculation from NeRF [51], we utilize the rasterization pipeline of Gaussians to compute the depth of each Gaussian primitive:

$$D_G = \sum_{i \in N} d_i \alpha_i T_i, \quad T_i = \prod_{j=1}^{i-1} (1 - \alpha_j), \quad (3)$$

where D_G is the rendered depth and d_i is the depth of each Gaussian splat in camera perspective.

It should be noted that the center of the Gaussian is not directly employed for depth computation. Due to variations in the shape and orientation of the Gaussian, the depth at the precise point where the ray intersects the Gaussian deviates from the depth at its center. Our approach computes the expected depth at the specific point of intersection with the Gaussian as follows:

$$d_i = \frac{1}{l} \left(p_2 - \frac{(\Sigma^{-1})_{0,2}}{(\Sigma^{-1})_{2,2}} (x_0 - p_0) - \frac{(\Sigma^{-1})_{1,2}}{(\Sigma^{-1})_{2,2}} (x_1 - p_1) \right) \quad (4)$$

where $\mathbf{p} = [p_0, p_1, p_2]$ represents the position of the Gaussian center in the ray space, and Σ is the 3×3 covariance matrix. $(\cdot)_{m,n}$ represents the corresponding element in the matrix. For detailed derivation and understanding of this process, please refer to Appendix.C.

Given the K captured views, we compute the depth loss using the following equation:

$$\mathcal{L}_{\text{depth}} = \sum_k \|D_G^k - D^k\|_1, \quad (5)$$

where D^k represents the inherent depth prior from LiDAR data.

The total loss function is as follows:

$$\mathcal{L}_{\text{total}} = \mathcal{L}_{\text{rgb}} + \lambda_{\text{depth}} \mathcal{L}_{\text{depth}}, \quad (6)$$

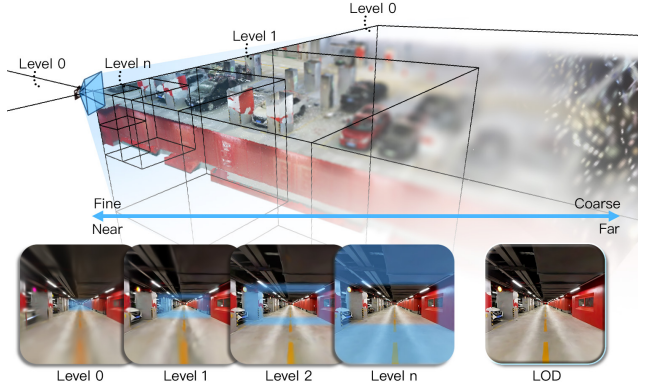


Figure 4: Illumination of our LOD-LiDAR-GS within an Octree Structure, accompanied by an LOD rendering strategy. Distance varies from near to far, with Gaussian level resolution transitioning from fine to coarse. The bottom row illustrates the level composition in the rendered view.

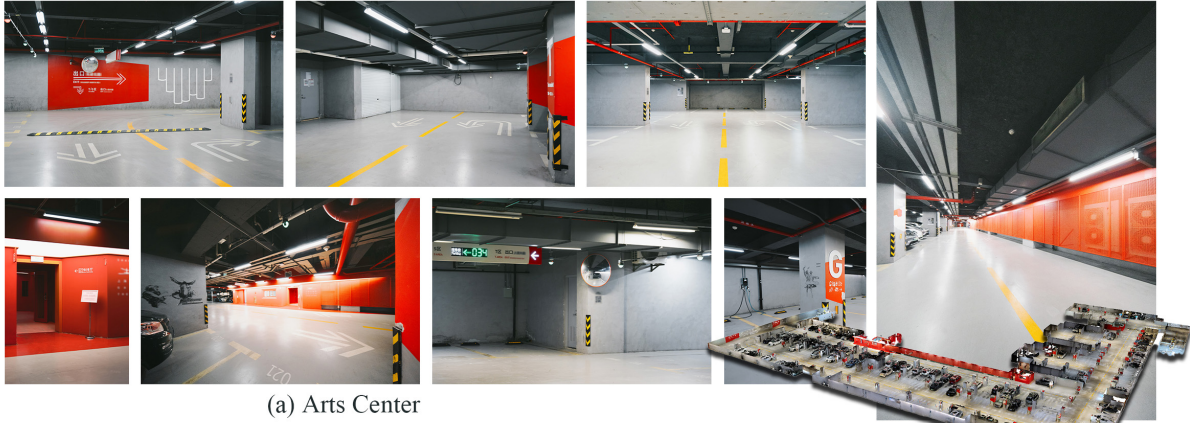
where \mathcal{L}_{rgb} is the RGB image reconstruction loss, following the original 3DGS, and λ_{depth} is the weight for our depth term. By incorporating the depth constraint, our LiDAR-GS effectively minimizes the occurrence of floating artifacts and aligns the Gaussian kernel more closely with the depth information inherent in the LiDAR data.

4.2. Multi-Resolution Representation

The original 3D Gaussian representation requires a vast number of 3D Gaussians, making it resource-intensive and inefficient for lightweight devices. However, simultaneously loading all Gaussians of the entire scene is inefficient and unnecessary for rendering a specific view.

Inspired by advanced rendering techniques [66] for massive LiDAR point clouds, we introduce a multi-resolution Gaussian framework called LOD-LiDAR-GS. This framework integrates the Level-of-Detail (LOD) rendering to the LiDAR-GS, making it suitable for various devices. We represent the 3D scene with Gaussians at different resolution levels. Each Gaussian has an additional LOD value, alongside its original attributes like 3D position, spherical harmonic coefficients, and opacity. The LOD value dynamically adjusts the cloning and splitting threshold during training. This multi-resolution representation enables fast and lightweight rendering on web-based devices.

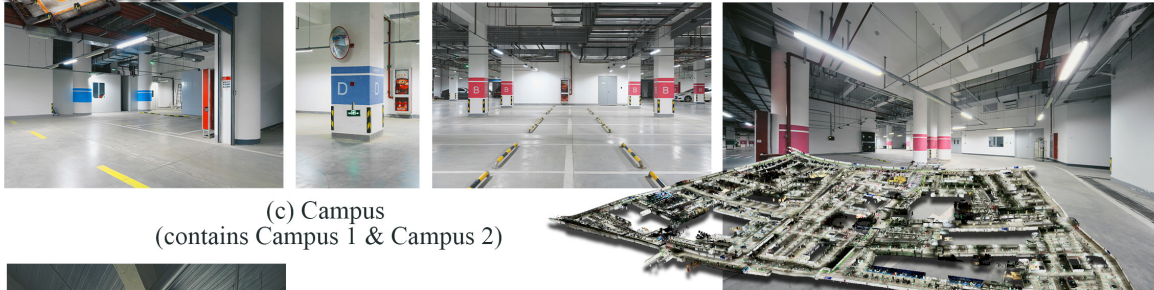
Multi-Resolution Gaussian Initialization. We first construct multi-resolution point cloud data for Gaussian initialization. Our Polar device generates dense point clouds with superior accuracy and consistency, even in challenging garage conditions. We use a spacing attribute, τ , to represent the resolution of a point cloud, defined as the minimal distance between points. The finest resolution corresponds to the original point cloud sampled from our reconstructed



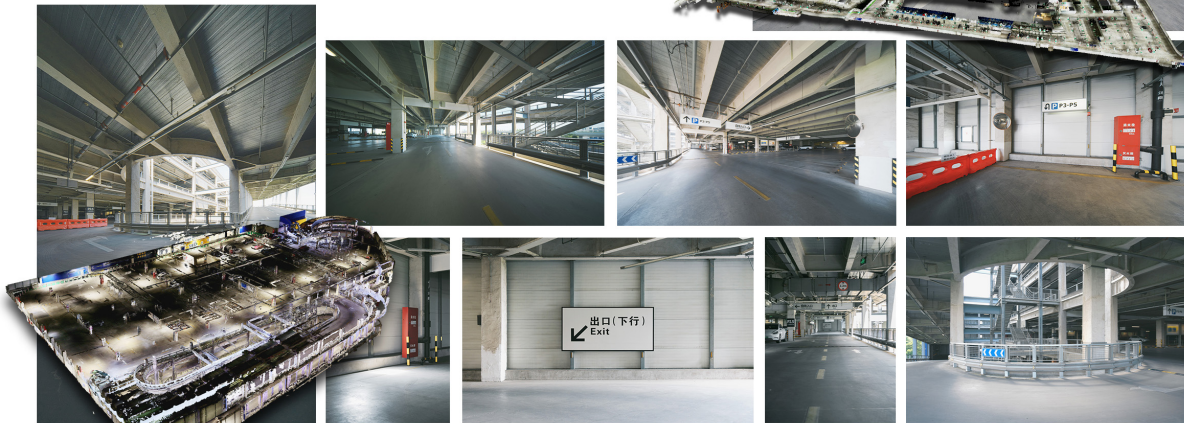
(a) Arts Center



(b) Shopping Mall 3



(c) Campus
(contains Campus 1 & Campus 2)



(d) Shopping Mall 1

Figure 5: Visualization of examples from our GarageWorld dataset.

mesh at the lowest τ . We then increase τ to 2τ and down-sample the point cloud to derive a coarser point cloud, repeating until the point count drops below a threshold, ϵ_p . Points in the finest level get an LOD value of $N = L - 1$, and those in the coarsest level get an LOD value of $N = 0$. We set τ to 4.0 cm and ϵ_p to 10,000 points. The down-sampling operation employs an approximate Poisson-disk sampling method from the PotreeConverter library [66].

LOD-LiDAR-GS Training. In contrast to LiDAR-GS, our LOD-LiDAR-GS framework processes a multi-resolution point cloud, wherein each resolution level has a distinct LOD value. We devise a new training strategy to handle the complexity caused by multi-resolution input effectively. We initialize a Gaussian model for each resolution level, which operates independently during optimization. Following the original 3DGS [34], the decision to clone or split a Gaussian is based on threshold values for position gradients σ_{pos} and variance σ_{var} . We introduce a scaling factor, s , which varies with the LOD value k of each level, modifying the thresholds as $s \cdot \sigma_{pos}$ and $s \cdot \sigma_{var}$:

$$s_k = \min(\beta_s^{L-1-k}, s_{max}), \quad k \in [0, L - 1] \quad (7)$$

where β_s and s_{max} are hyperparameters set to $\sqrt{2}$ and 4.0 respectively.

In our approach, the Gaussian representation at the lower resolution levels is employed to encapsulate the low-frequency content of the scene, while higher resolution levels utilize finer Gaussians to capture the intricate high-frequency details. To use our multi-resolution Gaussian models for image rendering, we adopt a technique analogous to LOD rendering used in traditional computer graphics pipelines. Gaussian subsets from each resolution level are selected based on the rendering camera’s viewing frustum and the projected depth d of each Gaussian. The appropriate Gaussian level $L^{(d)}$ is determined as:

$$L^{(d)} = \text{clamp}(\lfloor L^{1-d/d_{max}} \rfloor, 0, L - 1) \quad (8)$$

where d_{max} is the maximum depth value projected onto the training viewpoint from the point cloud.

During training, we select portions of Gaussians from different resolution levels based on depth ranges to accurately predict the image. We compute the loss by comparing model predictions with ground truth images. Our random-resolution-level (RRL) training strategy renders each training sample with a 50% probability using either the LOD strategy from multiple levels or a single Gaussian level, preventing overfitting and biases in camera pose distribution.

4.3. Web-based Lightweight Renderer

With the proposed multi-resolution Gaussian representation, our LOD-LiDAR-GS significantly enhances rendering efficiency. Instead of using a large number of 3D

ALGORITHM 1: Octree Construction for LOD-LiDAR-GS

```

Input : A set of multi-resolution Gaussians stored in .ply files
Output: Gaussian in Octree structure stored in .bin files

// Initialization
Create an octree with depth L
Compute bounding box B that covers all Gaussian levels
Initialize queue = {root of octree, B, lvl = 0}
// First loop: Distribute Gaussians into octree nodes
while length(queue) > 0 do
    currentNode ← queue.pop()
    foreach childNode of currentNode do
        Assign bounding box Bchild and
        lvl = {currentNode.lvl} + 1 to childNode
        queue.push({childNode, Bchild, lvl})
    end
    Read Gaussians from level_{currentNode.lvl}.ply
    Distribute Gaussians within currentNode.B
end
Initialize queue = {root of octree, B, lvl = 0}
byteOffset, byteSize = 0, 0
// Second loop: Prune empty nodes and store data
while length(queue) > 0 do
    currentNode ← queue.pop()
    foreach childNode of currentNode do
        if childNode.numPoints < 0 then
            queue.push({childNode, childNode.B, lvl})
        end
    end
    byteSize = size(currentNode.points)
    Flush currentNode.points into octree.bin file
    Flush currentNode.B,
    currentNode.numPoints, byteOffset,
    byteSize into hierarchy.bin file
    byteOffset ← byteOffset + byteSize
end

```

Gaussians for each image, LOD-LiDAR-GS dynamically selects Gaussian subsets from different resolution levels based on depth ranges. This reduces the complexity of sorting, projection, and accumulation operations, thereby accelerating rendering speed. On GPU systems such as the NVIDIA RTX3090, we implement a 3D Gaussian viewer based on the original 3DGS SIBR viewer. By integrating our LOD rendering strategy, as detailed in Equation 8, we achieve approximately a 4x increase in rendering speed. Additionally, we introduce a lightweight renderer employing an on-demand rendering approach. Unlike mainstream lightweight Gaussian renderers [39, 18], which load all Gaussians into VRAM simultaneously, our renderer dynamically loads only the necessary data into memory ac-

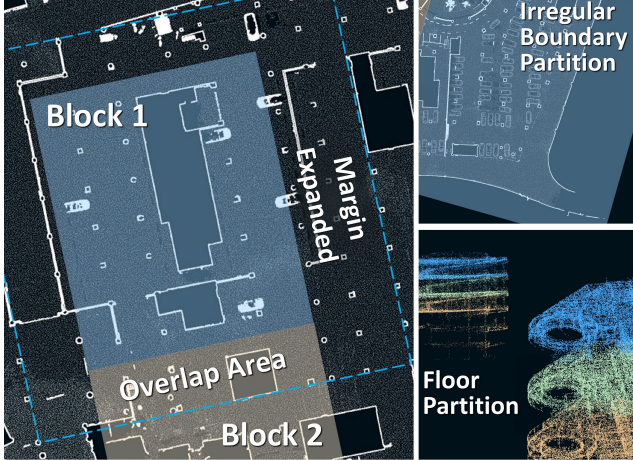


Figure 6: Illustration of our partition scheme. The left image shows the margin expansion method employed to guarantee overlap amongst the partitioned blocks. The top right image demonstrates the extension of partition boundaries to incorporate irregular areas. The bottom right image details the approach for multi-level parking structures, wherein each level is segregated into different partitions.

according to the current viewpoint and LOD strategy. This method avoids the need for full data loading, enabling the rendering of large-scale environments on web platforms.

Converting Multi-Resolution Gaussians into Octree Structure Our multi-resolution Gaussian representation is well-suited for storage within an Octree structure, with Gaussians at each level efficiently stored in the nodes at the corresponding depth of the Octree. We begin by constructing an Octree of depth L , where the root node host level 0 and the leaf nodes contain the finest level, $L - 1$. Intermediate levels are stored at the inner nodes of the Octree. We outline the conversion of our Gaussian representation into the Octree format in Algorithm 1.

Coarse-to-Fine Rendering Rendering large-scale garage scenes requires managing a substantial number of Gaussians, often exceeding in-memory storage capacity. To address this, we implement a coarse-to-fine loading and rendering scheme that facilitates real-time rendering on resource-constrained devices. Initially, low-resolution Gaussian levels are preloaded into memory at viewer initialization. These levels occupy minimal storage and are accessed frequently during subsequent rendering cycles. As shown in Fig. 4, to render high-frequency details, our system dynamically selects high-resolution octree chunks from disk based on the viewer’s frustum and the conditions set by our LOD rendering strategy, as outlined in Equation 8. The rendering process begins with a traversal of the entire oc-

tree, determining each node’s visibility based on the center position of the node’s bounding box. A second traversal then loads visible Gaussian data into a buffer, continuing until either the traversal is complete or the number of loaded Gaussians reaches the maximum capacity. The buffer is updated by replacing preloaded Gaussians with newly loaded high-resolution Gaussians, which are then dispatched to a WebGL worker for rendering. Recent works, such as OCT-GS [61] and LoG [70], can also be structured into an octree format. However, OCT-GS fails to represent the entire scene at certain levels, making it unsuitable for our lightweight rendering strategy. Additionally, LoG does not provide a solution for lightweight rendering.

5. Experimental Results

5.1. Training Details

All experiments are conducted on an NVIDIA RTX A6000 GPU using the PyTorch Framework. Given the large scale of our scenes and the initialization with LiDAR point clouds, we set the scaling learning rate to 0.0015 and the initial position learning rate for Gaussian primitives to 0.000016. We disable the opacity reset option and delay the start of the Gaussian densification step to 75,000 iterations. The total number of iterations is empirically set to twenty times the number of captured images. We use a spherical harmonics (SH) degree of 2 and set λ_{depth} to 0.8.

Block Partitioning and Merging. To accelerate our model training through parallel execution, we employ a partition-based strategy. As illustrated in Fig. 6, each garage floor is divided into sub-blocks using overlapping quadrilaterals, typically rectangles or trapezoids with small internal angles. Each block covers approximately 100 square meters, enabling efficient small-scale training for scene representation. To address the poor reconstruction quality at the edges, common in Gaussian splatting-based methods, we expand each quadrilateral outward by 30%. This expansion enhances the overall reconstruction quality. After training each partition, we merge the results using the original quadrilateral coordinates, achieving a complete scene reconstruction. This method ensures high-quality rendering while optimizing the training process.

Training Image Selection and Pre-processing. Regarding training view selection for each block, camera views originating within the partition bounds are retained. Furthermore, for camera views positioned outside the partition, we project the mesh in the partition block and the original mesh onto each camera view and compute the projected pixel overlap ratio between the quadrilateral-partitioned mesh and the whole mesh. Views with a ratio exceeding a

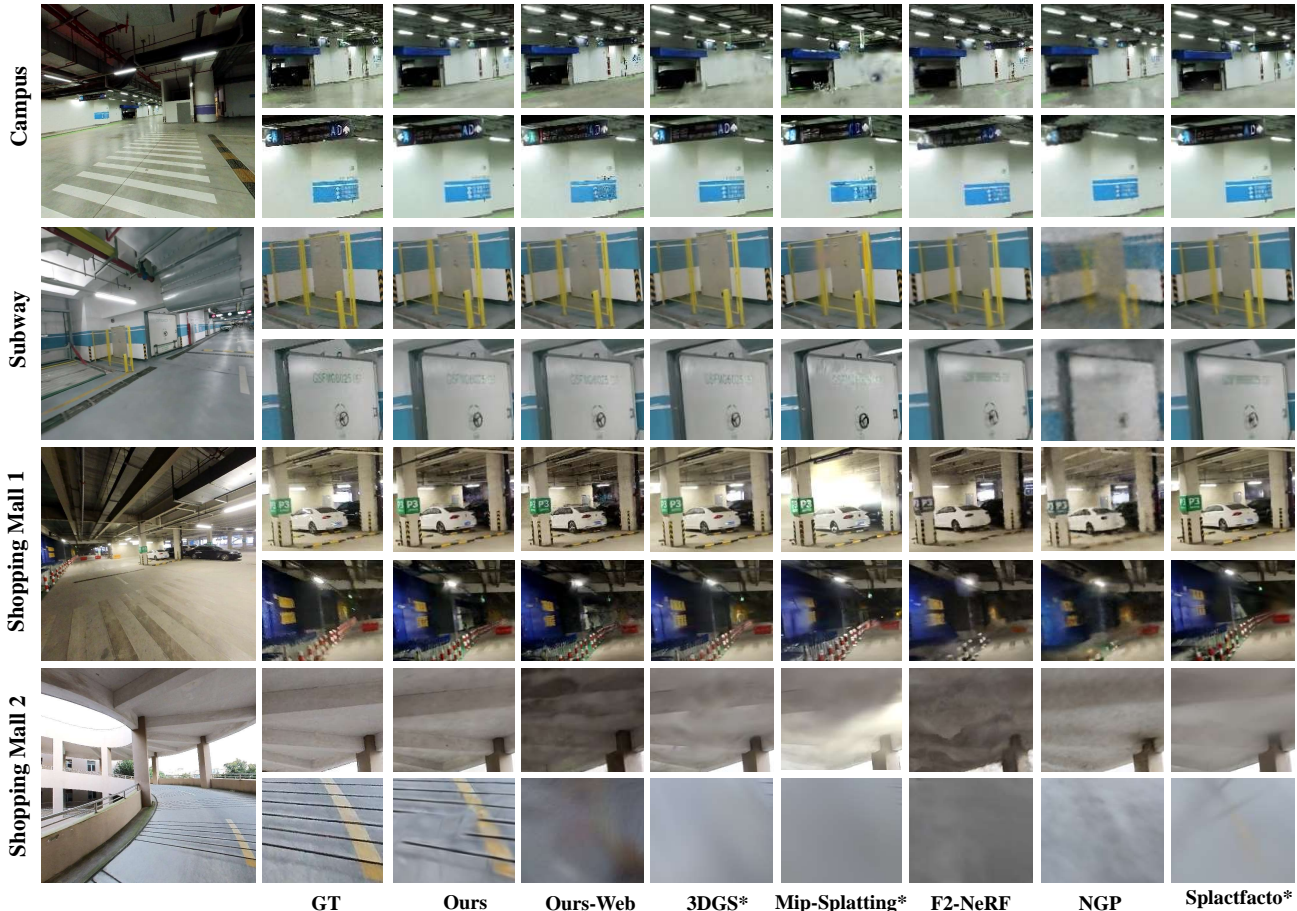


Figure 7: Qualitative comparison between our LOD-LiDAR-GS, 3DGS*, Mip-Splatting*, F2-NeRF, NGP and Splatfacto* on the various datasets. Here, we use a superscription * to denote their Gaussian primitives are initialized according to our LiDAR-assisted 3D point cloud.

Table 2: Quantitative comparison among our LOD-LiDAR-GS, 3DGS*, Mip-Splatting*, F2-NeRF, NGP, Splatfacto*, OCT-GS*, and LoG-GS* on the various datasets.

Method	GarageWorld			ScanNet++			KITTI-360		
	PSNR↑	SSIM↑	LPIPS↓	PSNR↑	SSIM↑	LPIPS↓	PSNR↑	SSIM↑	LPIPS↓
3DGS*	23.52	0.822	0.412	27.41	0.902	0.149	20.39	0.698	0.289
Mip-Splatting*	22.08	0.791	0.448	25.74	0.898	0.179	20.19	0.682	0.318
F2-NeRF	18.88	0.739	0.552	23.59	0.888	0.237	18.60	0.653	0.414
NGP	20.68	0.734	0.507	28.72	0.896	0.230	21.21	0.655	0.406
Splatfacto*	25.45	0.793	0.261	28.35	0.906	0.065	14.76	0.481	0.381
OCT-GS*	25.19	0.782	0.315	31.55	0.941	0.063	21.52	0.692	0.322
LoG-GS*	21.53	0.737	0.278	27.80	0.907	0.086	18.62	0.671	0.300
Ours(LOD-LiDAR-GS)	25.77	0.812	0.210	29.19	0.927	0.064	24.53	0.811	0.167
Ours(Web)	22.56	0.730	0.211	22.79	0.824	0.140	19.20	0.586	0.247

threshold of 0.8 are retained. The original Gaussian framework does not support direct input of fisheye images. To retain more information from the images, we avoided traditional fisheye distortion correction. Instead, we split a single fisheye image into five pinhole images. Specifically,

the fisheye image is projected onto a hemispherical surface. Then, five virtual cameras, each oriented at 45 degrees to the top, bottom, left, right, and straight ahead, reproject the hemispherical image into their respective views. This process generates new images and extrinsic parameters. Ad-

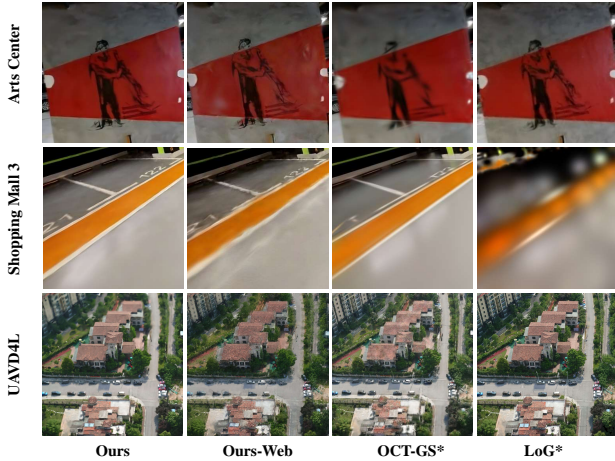


Figure 8: Qualitative comparison of our method and concurrent works, including recent OCT-GS* and LoG* methods, on the GarageWorld and UA4V4L datasets.

ditionally, since the downward-facing view includes part of the capturing device, we use a mask to obscure this portion of the image.

5.2. Comparison

Datasets. We compare our approach with state-of-the-art methods and concurrent works on various challenging datasets, including our **GarageWorld**, **KITTI-360** [44] (large outdoor street scene), and **ScanNet++** [92] (indoor scene characterized by complex geometry and variable lighting). For each dataset, we use 10% of the images as test sets and the remaining 90% as training sets.

Competing Methods We compare our method against a suite of 3DGS approaches, including **3DGS*** [34], **Mip-Splatting*** [94], and **Splactfacto*** [76], as well as recent concurrent work, including **OCT-GS*** [61] and **LoG*** [70]. Additionally, we benchmark our approach against recent implicit representation methods, namely **F2-NeRF** [81] and **Instant-NGP** [53]. To extend recent 3DGS-based methods to large-scale garage scenes, we initialize them with our LiDAR-derived point clouds instead of SFM point clouds, enabling their application to challenging garage environments. Methods utilizing our LiDAR-derived point clouds are denoted with an asterisk (*).

Quantitative Comparison Results. For quantitative comparisons, we use Peak Signal-to-Noise Ratio (PSNR), Structural Similarity (SSIM), and Learned Perceptual Image Patch Similarity (LPIPS)[96] as metrics to evaluate rendering quality. The results of these comparisons are presented in Tab. 2. Our LOD-LiDAR-GS method consistently achieves the best results on large-scale scene datasets, such

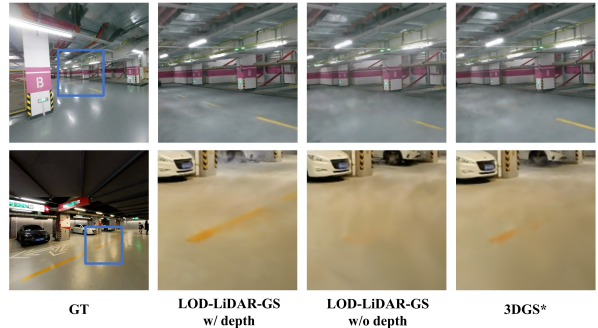


Figure 9: Qualitative ablation study on depth regularization within our large-scale GarageWorld dataset clearly demonstrates improvements in resolving the floater problem on the ground.

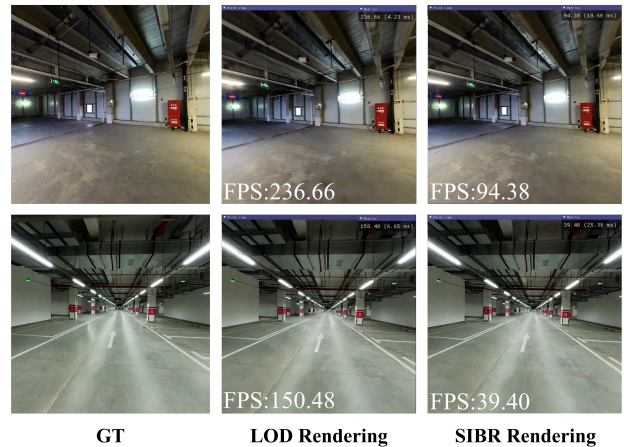


Figure 10: Ablation study on our LOD rendering strategy demonstrates that our real-time LOD renderer operates approximately 3-4 times faster than the original 3DGS SIBR viewer when tested on an NVIDIA RTX 3090 GPU.

as our GarageWorld dataset and the KITTI-360 dataset. On small-scale scene dataset ScanNet++, our LOD-LiDAR-GS approach achieves the second-best results. From the last two rows of Tab. 2, our web renderer demonstrate comparable performance on lightweight devices (MacBook Air with M2 clip).

Qualitative Comparison Results. As shown in Fig. 7, both 3DGS* and Splactfacto* tend to generate floating Gaussian points around scene surfaces, resulting in blurriness and poor rendering quality. F2-NeRF performs well on the relatively small-scale ScanNet++ dataset but suffers from artifacts in the large-scale KITTI-360 dataset and blurriness in our GarageWorld dataset. Instant-NGP, which utilizes hash encoding, produces notably blurry results in large-scale scenes. In contrast, our method demonstrates the

highest rendering quality across various scenarios. We also compared our method with concurrent works such as OCT-GS* and LoG*. As shown in Fig. 8, our approach achieves the best rendering quality on both our GarageWorld and the UAVD4L datasets (recently proposed and used in LoG*). Our web-based results also show comparable visual quality.

Rendering Performance of Web-based Renderer. Additionally, we evaluate the performance of our web-based renderer on various devices. On a high-performance desktop equipped with an i9-10900X CPU and a Samsung SSD T5 Disk, it takes 1.36 seconds to load approximately 2 million 3D Gaussians. On a MacBook laptop with an Apple M2 CPU and Apple SSD AP0512Z Disk, the load time for the same number of 3D Gaussians is 1.29 seconds. Combining these newly loaded 3D Gaussians with an additional 3 million pre-loaded Gaussians, both devices maintain a rendering frame rate of 60 FPS.

5.3. Ablation Study

In this section, we perform ablation studies to validate the effectiveness of each component of our approach.

Depth Regularization. Using only photometric loss constraints can easily produce artifacts, such as floaters, in large-scale scene reconstruction. To address this, we introduce an additional depth regularization term to enforce geometric constraints. As shown in Fig. 9, we evaluated the impact of our depth regularization module across various scenes. Our results demonstrate that the **LOD-LiDAR-GS** method effectively mitigates floaters on the ground when depth regularization is applied.

LOD Rendering Strategy. Next, we ablate the LOD rendering strategy. Based on our multi-resolution representation, we select Gaussian subsets from various resolution levels according to depth ranges, following the LOD rendering strategy outlined in Equation 8. This strategy significantly reduces the complexity of sorting, projection, and accumulation operations involved with 3D Gaussians, thereby accelerating the rendering speed. As shown in Fig. 10, our real-time viewer, integrated with the LOD rendering technique, is about 3-4 times faster than 3DGS’s SIBR viewer with similar rendering quality.

Random-Resolution-Level (RRL) Training Strategy. During training, directly applying the LOD rendering strategy to render images and optimize the loss can lead to overfitting at certain resolution levels in specific scene regions. We propose a random-resolution-level (RRL) training strategy to address this issue. As shown in Fig. 11, our RRL

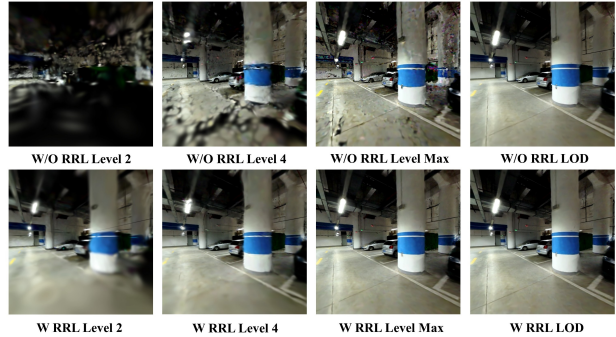


Figure 11: Qualitative ablation study on the random-resolution-level (RRL) training strategy reveals that our RRL approach effectively addresses the overfitting issue at a certain level, influenced by the camera distribution.

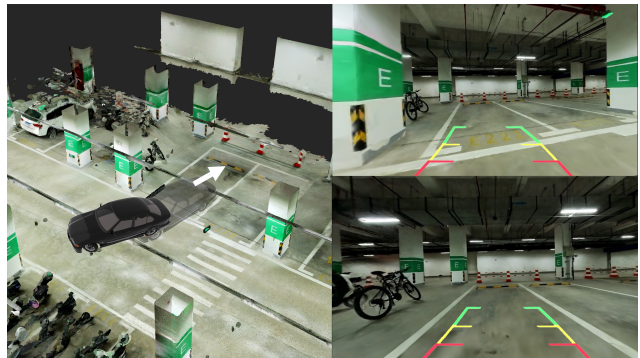


Figure 12: Autonomous vehicle parking. Our diverse garage scenes facilitate training algorithms for generating parking trajectories under different scenarios. When guiding the vehicle to the parking space, our garage model allows real-time and wide-FOV rendering of the environment, capturing drivable area and obstacles, thereby enhancing safe parking capabilities.

training strategy mitigates the overfitting problem and remains robust to variations in the distribution of input cameras.

6. GarageWorld

We introduce the first large-scale garage dataset, **GarageWorld**, captured with our Polar device. This dataset comprises eight large garages, featuring six underground garages, one outdoor parking lot, and one multi-floor indoor garage. These environments present diverse and intricate geometric structures, including sloped surfaces with distorted lines, internal circular paths, spiral ramps, and parked vehicles, as detailed in Table 1. Figure 5 visualizes the 3D models and rendered images of a subsection of these garages using our method. Our rendering pipeline and the GarageWorld dataset are designed to support a wide range

of applications, which are further detailed in the following sections.

Data Generation and Testbed for Autonomous Driving. Our developed 3D reconstruction of large-scale garage scenes with enhanced real-time rendering can support various autonomous driving algorithms. The GarageWorld dataset provides diverse driving scenarios, including tight parking spaces and complex geometric layouts, which are instrumental for training algorithms in autonomous parking and navigation path planning. Equipped with sensors such as LiDAR, IMU, and cameras, autonomous vehicles utilize these 3D structures for effective sensor fusion, enhancing their operational efficiency in varied garage environments. Additionally, our LetsGo pipeline further aids vehicle parking by supplementing sensor data, particularly in low-light garage conditions where camera and radar readings may be compromised. Our LiDAR-assisted Gaussian primitives allow rigorous testing in a virtual setting, prompting safe and efficient parking solutions. Fig. 12 illustrates how our approach generates rear-view images, allowing vehicles to accurately estimate distances and navigate tight spaces, thereby avoiding collisions and accelerating the development and deployment of safe autonomous driving technologies.

Real-time Localization and Navigation. Our LiDAR-assisted garage modeling and rendering significantly enhance autonomous vehicle localization and navigation by providing accurate 3D references that complement real-time sensor readings. In challenging indoor or underground garages, where GPS signals are typically unavailable, traditional localization methods encounter difficulties. Confined spaces and structured obstacles can cause interference for LiDAR and radar sensors, and multipath reflections can distort sensor readings. Low lighting conditions also reduce camera visibility, complicating vision-based localization. By integrating our Polar scanner with LiDAR-assisted Gaussian primitives, we offer accurately colored 3D references that enhance feature recognition and matching, significantly improving localization and navigation reliability. Figure 13 presents an example of real-time localization and navigation. Our system correlates captured images with our colored 3D models to compute relative poses and generate optimal paths through complex environments. During driving, our approach augments camera views and extends the vehicle’s field of view, ensuring comprehensive environmental awareness and safer navigation. Additionally, our web-based rendering engine represents expansive 3D garage maps and navigation trajectories on lightweight devices with limited computational capacity, delivering smooth real-time interactions and superior rendering performance.

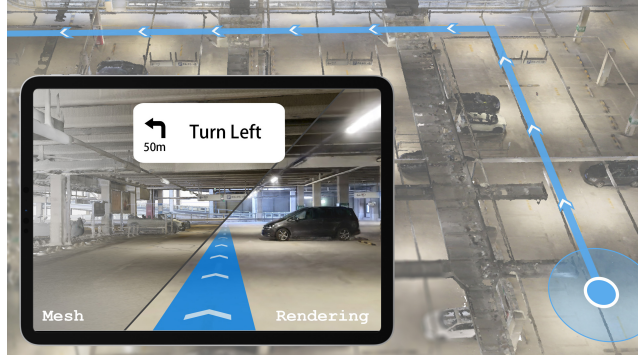


Figure 13: Real-time localization & navigation in challenging garage environments. Our colored 3D model facilitates precise vehicle camera localization and optimal path navigation, particularly in low-light garage conditions, ensuring safe driving. The lightweight web-based rendering ensures deployability in vehicles with limited computing resources.

VFX Production. Our reconstructed garage datasets and real-time rendering capabilities significantly enhance VFX production by providing a robust foundation for creating realistic backgrounds and seamlessly integrating CGI elements into live-action footage. Inspired by high-adrenaline sequences like the highway chase in “The Matrix Reloaded,” our LetsGo pipeline excels in modeling and rendering complex garage scenes. This capability allows for precise control over cinematic elements such as exposure time and motion blur, which are often challenging to manage on set. We created a VFX video production to showcase our technology using our reconstructed garage models (Fig. 14) in the supplementary video. We downloaded a video depicting highway chase scenes with dynamic viewing angles of a rapidly moving motorcycle. By extracting and aligning camera trajectories with our models and synthesizing motion blur, we created immersive visual effects that convincingly depict a chase within a garage environment. Our approach supports the exploration of diverse camera angles and compositions in real-time while ensuring visual consistency between real and virtual components, significantly reducing the need for reshoots and streamlining the production process. This integration empowers VFX artists to enhance the believability of scenes while conserving time and resources.

7. Limitations and Discussions

Although our rendering results exhibit commendable realism and we showcase various applications, our workflow still possesses certain limitations. Here we present a detailed analysis and explore further potential applications.

Firstly, our method focuses on large-scale garage scenes and relies on our lightweight 3D scanner to provide high-quality LiDAR point clouds, color images, and correspond-

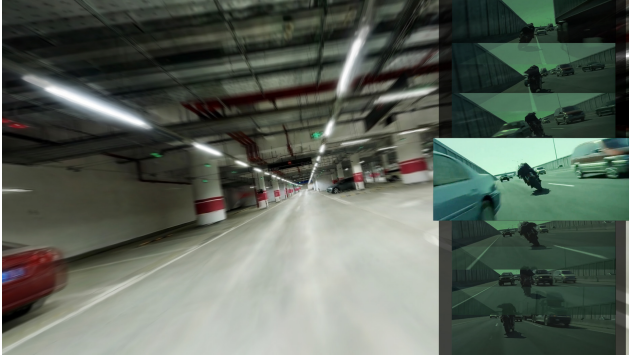


Figure 14: VFX demonstration. Through an analysis of the animation in the reference video, we extract the poses of several keyframes, which enable our system’s renderer to generate corresponding video segments. Our 3D garage modeling and rendering also enables motion blur rendering, producing realistic visual effects.

ing camera information. Although we have also validated the effectiveness of our method on other open-source datasets, it is important to explore the use of even lighter devices for scanning and rendering large-scale scenes, such as smartphones equipped with depth sensors. Additionally, we have currently collected data from eight large-scale garages, but it is necessary to gather more garage data to contribute to the community and facilitate further research on garage modeling and rendering.

As a method based on image rendering, our approach achieves highly realistic rendering effects, almost indistinguishable from real scenes. However, the existing pipeline does not support modifying lighting conditions. This requires us to carefully design the shooting process according to the lighting conditions, limiting the applicability of our method in various scenarios. Enabling rendering and editing of large-scale scenes under different lighting conditions is a meaningful direction that deserves further investigation. Our open-source dataset provides a foundation for the community to conduct research in these directions, allowing for advancements in this field.

Furthermore, there are additional directions and applications worth exploring. Inspired by SMERF [17], one potential research direction is to investigate streaming transmission methods for Gaussian kernels, enabling the distribution and on-the-fly rendering of large-scale scene data. Additionally, there are city generation methods such as InfiniCity [45] and CityDreamer [85], which leverage Generative Adversarial Networks (GANs) [26] to achieve rapid modeling of large-scale scenes. We intend to study large-scale scene generation based on 3D Gaussian representations. This fully explicit representation can be easily integrated into existing computer graphics workflows and achieve superior rendering effects.

8. Conclusion

For many of us, our daily lives begin with a safe departure from a garage and end with a safe arrival. The garage serves as the origin of our journey to innovation. This paper has contributed a handheld Polar device for data collection, a GarageWorld dataset, LiDAR-assisted Gaussian splatting for scene representation, and an LOD-based rendering technique that allows web-based rendering on consumer-level devices. Benefiting from these innovations, we successfully reconstruct various garages with diverse and challenging environments, allowing real-time rendering from any viewpoint on lightweight devices. Experimental results on the collected and two public datasets have demonstrated the effectiveness of our approach. Our GarageWorld, along with the reconstructed 3D model and real-time rendering, enables a set of applications, including training data generation and testbed for autonomous driving algorithms, real-time assistance for autonomous vehicle localization, navigation, and parking, as well as VFX production. Our current contributions mainly focus on the perception of the world, and it enables downstream recognition tasks. In the future, we will also explore garage generation, continuing to push the boundary of garage modeling and accomplishing a closure from perception, recognition, and generation.

References

- [1] S. Agarwal, Y. Furukawa, N. Snavely, I. Simon, B. Curless, S. M. Seitz, and R. Szeliski. Building rome in a day. *Communications of the ACM*, 54(10):105–112, 2011.
- [2] J. T. Barron, B. Mildenhall, M. Tancik, P. Hedman, R. Martin-Brualla, and P. P. Srinivasan. Mip-nerf: A multi-scale representation for anti-aliasing neural radiance fields. In *Proceedings of the IEEE/CVF International Conference on Computer Vision*, pages 5855–5864, 2021.
- [3] J. T. Barron, B. Mildenhall, D. Verbin, P. P. Srinivasan, and P. Hedman. Mip-nerf 360: Unbounded anti-aliased neural radiance fields. In *Proceedings of the IEEE/CVF Conference on Computer Vision and Pattern Recognition*, pages 5470–5479, 2022.
- [4] H. Bavle, J. L. Sanchez-Lopez, C. Cimarelli, A. Tourani, and H. Voos. From slam to situational awareness: Challenges and survey. *Sensors*, 23(10):4849, 2023.
- [5] M. Bujanca, X. Shi, M. Spear, P. Zhao, B. Lennox, and M. Luján. Robust slam systems: Are we there yet? In *2021 IEEE/RSJ International Conference on Intelligent Robots and Systems (IROS)*, pages 5320–5327. IEEE, 2021.
- [6] S. Ceriani, C. Sánchez, P. Taddei, E. Wolfart, and V. Sequiera. Pose interpolation slam for large maps using moving 3d sensors. In *2015 IEEE/RSJ international conference on intelligent robots and systems (IROS)*, pages 750–757. IEEE, 2015.
- [7] D. Charatan, S. Li, A. Tagliasacchi, and V. Sitzmann. pixelsplat: 3d gaussian splats from image pairs for scalable generalizable 3d reconstruction. In *arXiv*, 2023.

- [8] A. Chen, Z. Xu, A. Geiger, J. Yu, and H. Su. Tensorf: Tensorial radiance fields. In *European Conference on Computer Vision (ECCV)*, 2022.
- [9] A. Chen, Z. Xu, F. Zhao, X. Zhang, F. Xiang, J. Yu, and H. Su. Mvsnerf: Fast generalizable radiance field reconstruction from multi-view stereo. In *Proceedings of the IEEE/CVF International Conference on Computer Vision*, pages 14124–14133, 2021.
- [10] K. Cheng, X. Long, K. Yang, Y. Yao, W. Yin, Y. Ma, W. Wang, and X. Chen. Gaussianpro: 3d gaussian splatting with progressive propagation. *arXiv preprint arXiv:2402.14650*, 2024.
- [11] P. Cignoni, F. Ganovelli, E. Gobbetti, F. Marton, F. Ponghio, and R. Scopigno. Adaptive tetrapuzzles: efficient out-of-core construction and visualization of gigantic multiresolution polygonal models. *ACM Trans. Graph.*, 23(3):796–803, aug 2004.
- [12] D. Crandall, A. Owens, N. Snavely, and D. Huttenlocher. Discrete-continuous optimization for large-scale structure from motion. In *CVPR 2011*, pages 3001–3008. IEEE, 2011.
- [13] A. Dai, A. X. Chang, M. Savva, M. Halber, T. Funkhouser, and M. Nießner. Scannet: Richly-annotated 3d reconstructions of indoor scenes. In *Proceedings of the IEEE conference on computer vision and pattern recognition*, pages 5828–5839, 2017.
- [14] P. Dai, J. Xu, W. Xie, X. Liu, H. Wang, and W. Xu. High-quality surface reconstruction using gaussian surfels. In *SIGGRAPH 2024 Conference Papers*. Association for Computing Machinery, 2024.
- [15] Y. Dai, Z. Zhu, Z. Rao, and B. Li. Mvs2: Deep unsupervised multi-view stereo with multi-view symmetry. In *2019 International Conference on 3D Vision (3DV)*, pages 1–8. Ieee, 2019.
- [16] K. Deng, A. Liu, J.-Y. Zhu, and D. Ramanan. Depth-supervised NeRF: Fewer views and faster training for free. In *Proceedings of the IEEE/CVF Conference on Computer Vision and Pattern Recognition (CVPR)*, June 2022.
- [17] D. Duckworth, P. Hedman, C. Reiser, P. Zhizhin, J.-F. Thibert, M. Lučić, R. Szeliski, and J. T. Barron. Smerf: Streamable memory efficient radiance fields for real-time large-scene exploration, 2023.
- [18] H. Face. gsplat.js: Javascript gaussian splatting library. <https://github.com/huggingface/gsplat.js>, 2024. Accessed: 2024-05-15.
- [19] J.-M. Frahm, P. Fite-Georgel, D. Gallup, T. Johnson, R. Raguram, C. Wu, Y.-H. Jen, E. Dunn, B. Clipp, S. Lazebnik, et al. Building rome on a cloudless day. In *Computer Vision—ECCV 2010: 11th European Conference on Computer Vision, Heraklion, Crete, Greece, September 5-11, 2010, Proceedings, Part IV 11*, pages 368–381. Springer, 2010.
- [20] S. Fridovich-Keil, A. Yu, M. Tancik, Q. Chen, B. Recht, and A. Kanazawa. Plenoxels: Radiance fields without neural networks. In *Proceedings of the IEEE/CVF Conference on Computer Vision and Pattern Recognition*, pages 5501–5510, 2022.
- [21] P. Furgale, T. D. Barfoot, and G. Sibley. Continuous-time batch estimation using temporal basis functions. In *2012 IEEE International Conference on Robotics and Automation*, pages 2088–2095. IEEE, 2012.
- [22] P. Furgale, J. Rehder, and R. Siegwart. Unified temporal and spatial calibration for multi-sensor systems. In *2013 IEEE/RSJ International Conference on Intelligent Robots and Systems*, pages 1280–1286. IEEE, 2013.
- [23] Y. Furukawa, B. Curless, S. M. Seitz, and R. Szeliski. Towards internet-scale multi-view stereo. In *2010 IEEE Computer Society Conference on Computer Vision and Pattern Recognition*, pages 1434–1441, 2010.
- [24] Y. Furukawa and J. Ponce. Accurate, dense, and robust multiview stereopsis. *IEEE Transactions on Pattern Analysis and Machine Intelligence*, 32(8):1362–1376, 2010.
- [25] M. Goesele, N. Snavely, B. Curless, H. Hoppe, and S. M. Seitz. Multi-view stereo for community photo collections. In *2007 IEEE 11th International Conference on Computer Vision*, pages 1–8. IEEE, 2007.
- [26] I. Goodfellow, J. Pouget-Abadie, M. Mirza, B. Xu, D. Warde-Farley, S. Ozair, A. Courville, and Y. Bengio. Generative adversarial nets. *Advances in neural information processing systems*, 27, 2014.
- [27] A. Guédon and V. Lepetit. Sugar: Surface-aligned gaussian splatting for efficient 3d mesh reconstruction and high-quality mesh rendering. *arXiv preprint arXiv:2311.12775*, 2023.
- [28] J. Heinly, J. L. Schonberger, E. Dunn, and J.-M. Frahm. Reconstructing the world* in six days*(as captured by the yahoo 100 million image dataset). In *Proceedings of the IEEE conference on computer vision and pattern recognition*, pages 3287–3295, 2015.
- [29] B. Huang, H. Yi, C. Huang, Y. He, J. Liu, and X. Liu. M3vsnet: Unsupervised multi-metric multi-view stereo network. In *2021 IEEE International Conference on Image Processing (ICIP)*, pages 3163–3167. IEEE, 2021.
- [30] B. Huang, Z. Yu, A. Chen, A. Geiger, and S. Gao. 2d gaussian splatting for geometrically accurate radiance fields. *SIGGRAPH*, 2024.
- [31] Y. Jiang, Z. Shen, P. Wang, Z. Su, Y. Hong, Y. Zhang, J. Yu, and L. Xu. Hifi4g: High-fidelity human performance rendering via compact gaussian splatting, 2023.
- [32] M. Kazhdan, M. Bolitho, and H. Hoppe. Poisson surface reconstruction. In *Proceedings of the fourth Eurographics symposium on Geometry processing*, volume 7, page 0, 2006.
- [33] N. Keetha, J. Karhade, K. M. Jatavallabhula, G. Yang, S. Scherer, D. Ramanan, and J. Luiten. Splatam: Splat, track & map 3d gaussians for dense rgb-d slam. In *Proceedings of the IEEE/CVF Conference on Computer Vision and Pattern Recognition*, 2024.
- [34] B. Kerbl, G. Kopanas, T. Leimkühler, and G. Drettakis. 3d gaussian splatting for real-time radiance field rendering. *ACM Transactions on Graphics*, 42(4), July 2023.
- [35] B. Kerbl, A. Meuleman, G. Kopanas, M. Wimmer, A. Lanvin, and G. Drettakis. A hierarchical 3d gaussian representation for real-time rendering of very large datasets. *ACM Transactions on Graphics*, 43(4), July 2024.

- [36] J. Kerr, C. M. Kim, K. Goldberg, A. Kanazawa, and M. Tancik. Lrf: Language embedded radiance fields. In *Proceedings of the IEEE/CVF International Conference on Computer Vision*, pages 19729–19739, 2023.
- [37] A. Kirillov, E. Mintun, N. Ravi, H. Mao, C. Rolland, L. Gustafson, T. Xiao, S. Whitehead, A. C. Berg, W.-Y. Lo, P. Dollar, and R. Girshick. Segment anything. In *Proceedings of the IEEE/CVF International Conference on Computer Vision (ICCV)*, pages 4015–4026, October 2023.
- [38] J. Kulhanek and T. Sattler. Tetra-nerf: Representing neural radiance fields using tetrahedra. *arXiv preprint arXiv:2304.09987*, 2023.
- [39] K. Kwok. splat. <https://github.com/antimatter15/splat>, 2023. Accessed: 2024-05-15.
- [40] J. J. Leonard and H. F. Durrant-Whyte. Simultaneous map building and localization for an autonomous mobile robot. In *IROS*, volume 3, pages 1442–1447, 1991.
- [41] J. Li, Z. Lu, Y. Wang, Y. Wang, and J. Xiao. Ds-mvsnet: Unsupervised multi-view stereo via depth synthesis. In *Proceedings of the 30th ACM International Conference on Multimedia*, pages 5593–5601, 2022.
- [42] J. Li, L. Pei, D. Zou, S. Xia, Q. Wu, T. Li, Z. Sun, and W. Yu. Attention-slam: A visual monocular slam learning from human gaze. *IEEE Sensors Journal*, 21(5):6408–6420, 2020.
- [43] J. Li, J. Zhang, X. Bai, J. Zheng, X. Ning, J. Zhou, and L. Gu. Dngaussian: Optimizing sparse-view 3d gaussian radiance fields with global-local depth normalization. *arXiv preprint arXiv:2403.06912*, 2024.
- [44] Y. Liao, J. Xie, and A. Geiger. Kitti-360: A novel dataset and benchmarks for urban scene understanding in 2d and 3d. *IEEE Transactions on Pattern Analysis and Machine Intelligence*, 45(3):3292–3310, 2022.
- [45] C. H. Lin, H.-Y. Lee, W. Menapace, M. Chai, A. Siarohin, M.-H. Yang, and S. Tulyakov. InfiniCity: Infinite-scale city synthesis. In *Proceedings of the IEEE/CVF international conference on computer vision*, 2023.
- [46] J. Lin, Z. Li, X. Tang, J. Liu, S. Liu, J. Liu, Y. Lu, X. Wu, S. Xu, Y. Yan, and W. Yang. Vastgaussian: Vast 3d gaussians for large scene reconstruction. In *CVPR*, 2024.
- [47] Y. Liu, H. Guan, C. Luo, L. Fan, J. Peng, and Z. Zhang. Citygaussian: Real-time high-quality large-scale scene rendering with gaussians. *arXiv preprint arXiv:2404.01133*, 2024.
- [48] T. Lu, M. Yu, L. Xu, Y. Xiangli, L. Wang, D. Lin, and B. Dai. Scaffold-gs: Structured 3d gaussians for view-adaptive rendering. *Conference on Computer Vision and Pattern Recognition (CVPR)*, 2024.
- [49] H. Matsuki, R. Murai, P. H. J. Kelly, and A. J. Davison. Gaussian Splatting SLAM. 2024.
- [50] J. Maye, P. Furgale, and R. Siegwart. Self-supervised calibration for robotic systems. In *2013 IEEE Intelligent Vehicles Symposium (IV)*, pages 473–480. IEEE, 2013.
- [51] B. Mildenhall, P. P. Srinivasan, M. Tancik, J. T. Barron, R. Ramamoorthi, and R. Ng. Nerf: Representing scenes as neural radiance fields for view synthesis. *Communications of the ACM*, 65(1):99–106, 2021.
- [52] P. Moulon, P. Monasse, and R. Marlet. Adaptive structure from motion with a contrario model estimation. In *Computer Vision—ACCV 2012: 11th Asian Conference on Computer Vision, Daejeon, Korea, November 5-9, 2012, Revised Selected Papers, Part IV 11*, pages 257–270. Springer, 2013.
- [53] T. Müller, A. Evans, C. Schied, and A. Keller. Instant neural graphics primitives with a multiresolution hash encoding. *ACM Transactions on Graphics (ToG)*, 41(4):1–15, 2022.
- [54] S. Niedermayr, J. Stumpfegger, and R. Westermann. Compressed 3d gaussian splatting for accelerated novel view synthesis. *arXiv preprint arXiv:2401.02436*, 2023.
- [55] A. Noguchi, X. Sun, S. Lin, and T. Harada. Neural articulated radiance field. In *Proceedings of the IEEE/CVF International Conference on Computer Vision*, pages 5762–5772, 2021.
- [56] L. Oth, P. Furgale, L. Kneip, and R. Siegwart. Rolling shutter camera calibration. In *Proceedings of the IEEE Conference on Computer Vision and Pattern Recognition*, pages 1360–1367, 2013.
- [57] F. Ponchio and M. Dellepiane. Multiresolution and fast decompression for optimal web-based rendering. *Graph. Model.*, 88:1–11, 2016.
- [58] D. Rebain, W. Jiang, S. Yazdani, K. Li, K. M. Yi, and A. Tagliasacchi. Derf: Decomposed radiance fields. In *Proceedings of the IEEE/CVF Conference on Computer Vision and Pattern Recognition*, pages 14153–14161, 2021.
- [59] J. Rehder, J. Nikolic, T. Schneider, T. Hinzmann, and R. Siegwart. Extending kalibr: Calibrating the extrinsics of multiple imus and of individual axes. In *2016 IEEE International Conference on Robotics and Automation (ICRA)*, pages 4304–4311. IEEE, 2016.
- [60] K. Rematas, A. Liu, P. P. Srinivasan, J. T. Barron, A. Tagliasacchi, T. Funkhouser, and V. Ferrari. Urban radiance fields. In *Proceedings of the IEEE/CVF Conference on Computer Vision and Pattern Recognition*, pages 12932–12942, 2022.
- [61] K. Ren, L. Jiang, T. Lu, M. Yu, L. Xu, Z. Ni, and B. Dai. Octree-gs: Towards consistent real-time rendering with lod-structured 3d gaussians. *arXiv preprint arXiv:2403.17898*, 2024.
- [62] B. Roessle, J. T. Barron, B. Mildenhall, P. P. Srinivasan, and M. Nießner. Dense depth priors for neural radiance fields from sparse input views. In *Proceedings of the IEEE/CVF Conference on Computer Vision and Pattern Recognition (CVPR)*, June 2022.
- [63] J. Schauer and A. Nüchter. The peoplere mover—removing dynamic objects from 3-d point cloud data by traversing a voxel occupancy grid. *IEEE robotics and automation letters*, 3(3):1679–1686, 2018.
- [64] P. Schmuck, T. Ziegler, M. Karrer, J. Perraudin, and M. Chli. Covins: Visual-inertial slam for centralized collaboration. In *2021 IEEE International Symposium on Mixed and Augmented Reality Adjunct (ISMAR-Adjunct)*, pages 171–176. IEEE, 2021.
- [65] J. L. Schonberger and J.-M. Frahm. Structure-from-motion revisited. In *Proceedings of the IEEE conference on com-*

- puter vision and pattern recognition, pages 4104–4113, 2016.
- [66] M. Schütz et al. Potree: Rendering large point clouds in web browsers. *Technische Universität Wien, Wien*, 2016.
- [67] M. Schütz, S. Ohrhallinger, and M. Wimmer. Fast out-of-core octree generation for massive point clouds. In *Computer Graphics Forum*, volume 39, pages 155–167. Wiley Online Library, 2020.
- [68] S. M. Seitz, B. Curless, J. Diebel, D. Scharstein, and R. Szeliski. A comparison and evaluation of multi-view stereo reconstruction algorithms. In *2006 IEEE computer society conference on computer vision and pattern recognition (CVPR'06)*, volume 1, pages 519–528. IEEE, 2006.
- [69] T. Shan, B. Englot, C. Ratti, and D. Rus. Lvi-sam: Tightly-coupled lidar-visual-inertial odometry via smoothing and mapping. In *2021 IEEE international conference on robotics and automation (ICRA)*, pages 5692–5698. IEEE, 2021.
- [70] Q. Shuai, H. Guo, Z. Xu, H. Lin, S. Peng, H. Bao, and X. Zhou. Real-time view synthesis for large scenes with millions of square meters. 2024.
- [71] N. Snavely, S. M. Seitz, and R. Szeliski. Skeletal graphs for efficient structure from motion. In *2008 IEEE Conference on Computer Vision and Pattern Recognition*, pages 1–8. IEEE, 2008.
- [72] C. Sun, M. Sun, and H. Chen. Direct voxel grid optimization: Super-fast convergence for radiance fields reconstruction. In *CVPR*, 2022.
- [73] W. Sun, E. Trulls, Y.-C. Tseng, S. Sumbandam, G. Sharma, A. Tagliasacchi, and K. M. Yi. Pointnerf++: A multi-scale, point-based neural radiance field. *arXiv preprint arXiv:2312.02362*, 2023.
- [74] C. Sweeney, V. Fragoso, T. Höllerer, and M. Turk. Large scale sfm with the distributed camera model. In *2016 Fourth International Conference on 3D Vision (3DV)*, pages 230–238. IEEE, 2016.
- [75] M. Tancik, V. Casser, X. Yan, S. Pradhan, B. Mildenhall, P. P. Srinivasan, J. T. Barron, and H. Kretschmar. Blocknerf: Scalable large scene neural view synthesis. In *Proceedings of the IEEE/CVF Conference on Computer Vision and Pattern Recognition*, pages 8248–8258, 2022.
- [76] M. Tancik, E. Weber, E. Ng, R. Li, B. Yi, J. Kerr, T. Wang, A. Kristoffersen, J. Austin, K. Salahi, A. Ahuja, D. McAllister, and A. Kanazawa. Nerfstudio: A modular framework for neural radiance field development. In *ACM SIGGRAPH 2023 Conference Proceedings, SIGGRAPH '23*, 2023.
- [77] J. Tang, J. Ren, H. Zhou, Z. Liu, and G. Zeng. Dreamgaussian: Generative gaussian splatting for efficient 3d content creation. *arXiv preprint arXiv:2309.16653*, 2023.
- [78] Z. Teed and J. Deng. Droid-slam: Deep visual slam for monocular, stereo, and rgb-d cameras. *Advances in neural information processing systems*, 34:16558–16569, 2021.
- [79] H. Turki, D. Ramanan, and M. Satyanarayanan. Meganerf: Scalable construction of large-scale nerfs for virtual fly-throughs. In *Proceedings of the IEEE/CVF Conference on Computer Vision and Pattern Recognition*, pages 12922–12931, 2022.
- [80] M. Turkulainen, X. Ren, I. Melekhov, O. Seiskari, E. Rahtu, and J. Kannala. Dn-splatter: Depth and normal priors for gaussian splatting and meshing, 2024.
- [81] P. Wang, Y. Liu, Z. Chen, L. Liu, Z. Liu, T. Komura, C. Theobalt, and W. Wang. F2-nerf: Fast neural radiance field training with free camera trajectories. In *Proceedings of the IEEE/CVF Conference on Computer Vision and Pattern Recognition*, pages 4150–4159, 2023.
- [82] C. Wu. Towards linear-time incremental structure from motion. In *2013 International Conference on 3D Vision-3DV 2013*, pages 127–134. IEEE, 2013.
- [83] G. Wu, T. Yi, J. Fang, L. Xie, X. Zhang, W. Wei, W. Liu, Q. Tian, and X. Wang. 4d gaussian splatting for real-time dynamic scene rendering. *arXiv preprint arXiv:2310.08528*, 2023.
- [84] X. Wu, J. Xu, X. Zhang, H. Bao, Q. Huang, Y. Shen, J. Tompkin, and W. Xu. Scanerf: Scalable bundle-adjusting neural radiance fields for large-scale scene rendering. *ACM Transactions on Graphics (TOG)*, 42(6):1–18, 2023.
- [85] H. Xie, Z. Chen, F. Hong, and Z. Liu. Citydreamer: Compositional generative model of unbounded 3d cities. *arXiv preprint arXiv:2309.00610*, 2023.
- [86] H. Xu, Z. Zhou, Y. Qiao, W. Kang, and Q. Wu. Self-supervised multi-view stereo via effective co-segmentation and data-augmentation. In *Proceedings of the AAAI Conference on Artificial Intelligence*, volume 35, pages 3030–3038, 2021.
- [87] H. Xu, Z. Zhou, Y. Wang, W. Kang, B. Sun, H. Li, and Y. Qiao. Digging into uncertainty in self-supervised multi-view stereo. In *Proceedings of the IEEE/CVF International Conference on Computer Vision*, pages 6078–6087, 2021.
- [88] Q. Xu, Z. Xu, J. Philip, S. Bi, Z. Shu, K. Sunkavalli, and U. Neumann. Point-nerf: Point-based neural radiance fields. In *Proceedings of the IEEE/CVF Conference on Computer Vision and Pattern Recognition*, pages 5438–5448, 2022.
- [89] Y. Yan, H. Lin, C. Zhou, W. Wang, H. Sun, K. Zhan, X. Lang, X. Zhou, and S. Peng. Street gaussians for modeling dynamic urban scenes, 2024.
- [90] J. Yang, J. M. Alvarez, and M. Liu. Self-supervised learning of depth inference for multi-view stereo. In *Proceedings of the IEEE/CVF Conference on Computer Vision and Pattern Recognition*, pages 7526–7534, 2021.
- [91] Y. Yao, Z. Luo, S. Li, T. Fang, and L. Quan. Mvsnet: Depth inference for unstructured multi-view stereo. In *Proceedings of the European conference on computer vision (ECCV)*, pages 767–783, 2018.
- [92] C. Yeshwanth, Y.-C. Liu, M. Nießner, and A. Dai. Scannet++: A high-fidelity dataset of 3d indoor scenes. In *Proceedings of the IEEE/CVF International Conference on Computer Vision*, pages 12–22, 2023.
- [93] A. Yu, V. Ye, M. Tancik, and A. Kanazawa. pixelnerf: Neural radiance fields from one or few images. In *Proceedings of the IEEE/CVF Conference on Computer Vision and Pattern Recognition*, pages 4578–4587, 2021.
- [94] Z. Yu, A. Chen, B. Huang, T. Sattler, and A. Geiger. Mip-splatting: Alias-free 3d gaussian splatting. *arXiv:2311.16493*, 2023.

- [95] K. Zhang, G. Riegler, N. Snively, and V. Koltun. Nerf++: Analyzing and improving neural radiance fields. *arXiv preprint arXiv:2010.07492*, 2020.
- [96] R. Zhang, P. Isola, A. A. Efros, E. Shechtman, and O. Wang. The unreasonable effectiveness of deep features as a perceptual metric. In *Proceedings of the IEEE conference on computer vision and pattern recognition*, pages 586–595, 2018.
- [97] F. Zhao, Y. Jiang, K. Yao, J. Zhang, L. Wang, H. Dai, Y. Zhong, Y. Zhang, M. Wu, L. Xu, et al. Human performance modeling and rendering via neural animated mesh. *ACM Transactions on Graphics (TOG)*, 41(6):1–17, 2022.
- [98] F. Zhao, W. Yang, J. Zhang, P. Lin, Y. Zhang, J. Yu, and L. Xu. Humannerf: Efficiently generated human radiance field from sparse inputs. In *Proceedings of the IEEE/CVF Conference on Computer Vision and Pattern Recognition*, pages 7743–7753, 2022.
- [99] X. Zhou, Z. Lin, X. Shan, Y. Wang, D. Sun, and M.-H. Yang. Drivinggaussian: Composite gaussian splatting for surrounding dynamic autonomous driving scenes. *arXiv preprint arXiv:2312.07920*, 2023.
- [100] M. Zwicker, H. Pfister, J. van Baar, and M. Gross. Ewa volume splatting. In *Proceedings Visualization, 2001. VIS '01.*, pages 29–538, 2001.
- [101] M. Zwicker, H. Pfister, J. Van Baar, and M. Gross. Surface splatting. In *Proceedings of the 28th annual conference on Computer graphics and interactive techniques*, pages 371–378, 2001.

A. Specifications and Calibration of Polar Device

Below, we provide the configuration and calibration details of our Polar scanner. The data acquisition unit comprises an Ouster OS0-128 REV6 LiDAR, an Insta360 ONE RS 1-inch 360 Edition Camera, and an Xsens MTi-630 IMU. Time synchronization across sensors is achieved using DEITY TC-1 timecode generators and simulated analog GPS NMEA time signals. The data collection unit and processing unit weigh 1250g and 850g, respectively, excluding the battery. The total apparatus weight does not exceed 3.2 kg, making it ideal for both handheld and wearable scanning applications. Additionally, we have engineered an over-shoulder support system to enhance operator stability during scans.

For the intrinsic parameter calibration of the fisheye camera and the IMU sensor, we leverage the program provided by OpenCV and the Allan Variance ROS toolbox [59, 22, 21, 50, 56], respectively. The extrinsic calibration between the fisheye camera and the IMU uses the Kalibr calibration program [59]. Due to the sparsity, noisiness, and uncolored nature of the point cloud data collected by our LiDAR sensor, it is hard to establish correspondences between the LiDAR data and the images captured by the fisheye camera, making relative pose estimation between the sensors difficult. To address this issue, we intro-

duce an additional sensor, a FARO laser scanner. This scanner provides dense, accurate, and colored point clouds and thus functions as a bridge for the relative pose estimation between the LiDAR sensor and the fisheye camera. Specifically, we adopt a checkerboard as our calibration scene and capture data from it using the FARO laser scanner and Polar device. The relative pose between the FARO laser scanner and the LiDAR sensor in our Polar device is achieved by point cloud registration, and that between the FARO laser scanner and the fisheye camera is obtained by establishing color correspondences between the point cloud captured by the FARO sensor and the fisheye image. By connecting the transformation from FARO to LiDAR and from FARO to the fisheye camera, we can finally calculate the extrinsic parameters between the LiDAR and the fisheye camera. We repeat this process twelve times in our implementation to reduce experimental error. It is important to note that FARO was only used to calibrate between the fisheye camera and the LiDAR **before** we start scanning a garage, and the process only needs to be conducted once.

B. Data Preprocessing and Mesh cleanup

To ensure data privacy, we anonymized vehicle license plate information recorded in the underground garage data collection. Specifically, we used image blurring to hide license plate numbers from identification. This step is essential to protect individual privacy and comply with data protection regulations. To remove the dynamic objects in the collected data, we apply Segment Anything [37] to the images. For the point cloud data, we estimate whether the points scanned at one LiDAR frame are also observed at other frames, similar to Schauer and Nüchter [63]. For mesh cleaning, we construct a kd-tree from the point cloud of LIV-SLAM and calculate the nearest neighbour distance of each mesh face ($k = 1$). If the distance exceeds 0.1m, we remove the face.

C. Details of depth calculation

To accurately calculate depth, we treat each Gaussian as a probability density function. Following [100], we get the depth of each Gaussian primitive, d_i , by calculating the expected value of depth under this probability density as:

$$d_i = \frac{\int_{-\infty}^{+\infty} t g_i(\mathbf{x}) dx_2}{\int_{-\infty}^{+\infty} g_i(\mathbf{x}) dx_2} = \frac{1}{l} \frac{\int_{-\infty}^{+\infty} x_2 g_i(x_2 | x_0, x_1) dx_2}{\int_{-\infty}^{+\infty} g_i(x_2 | x_0, x_1) dx_2}, \quad (9)$$

where g_i is the Gaussian function, $\mathbf{x} = [x_0, x_1, x_2]^T$ is the coordinate of the space in the ray space, where x_0, x_1 are the pixel coordinates, x_2 is oriented in the same direction as the pixel ray. As in [100], $t = x_2/l$ is the depth of \mathbf{x} in the camera coordinate system and $l = \sqrt{x_0^2 + x_1^2 + 1}$. We denote the center of the Gaussian in ray space as $\mathbf{p} =$

$[p_0, p_1, p_2]$ and the covariance matrix as Σ , by defining $\mathbf{y} = \mathbf{x} - \mathbf{p}$, the Eqn. 9 can be simplified as:

$$\begin{aligned} d_i &= \frac{1}{l} \frac{\int_{-\infty}^{+\infty} (y_2 + p_2) g_i(\mathbf{y} + \mathbf{p}) dx_2}{\int_{-\infty}^{+\infty} g_i(\mathbf{y} + \mathbf{p}) dx_2} \\ &= \frac{1}{l} \left(p_2 + \frac{\int_{-\infty}^{+\infty} y_2 g_i(\mathbf{y} + \mathbf{p}) dy_2}{\int_{-\infty}^{+\infty} g_i(\mathbf{y} + \mathbf{p}) dy_2} \right). \end{aligned} \quad (10)$$

Then, $g(\mathbf{y} + \mathbf{p})$ can be expanded as:

$$g(\mathbf{y} + \mathbf{p}) = e^{-Ay_2^2 + By_2 + C} = e^C \cdot e^{-Ay_2^2 + By_2}, \quad (11)$$

where

$$\begin{aligned} A &= \frac{1}{2} (\Sigma^{-1})_{2,2} \\ B &= -(\Sigma^{-1})_{2,0} y_0 - (\Sigma^{-1})_{2,1} y_1 \\ C &= -\frac{1}{2} (\Sigma^{-1})_{0,0} y_0^2 - \frac{1}{2} (\Sigma^{-1})_{1,1} y_1^2 - (\Sigma^{-1})_{1,0} y_0 y_1 \\ &\dots \end{aligned} \quad (12)$$

By integrating an arbitrary Gaussian function, we obtain:

$$\int_{-\infty}^{+\infty} e^{-Au^2 + Bu} du = \sqrt{\frac{\pi}{A}} e^{\frac{B^2}{4A}}, \quad (13)$$

$$\int_{-\infty}^{+\infty} u e^{-Au^2 + Bu} du = \frac{B}{2A} \sqrt{\frac{\pi}{A}} e^{\frac{B^2}{4A}}. \quad (14)$$

Next, substituting Eqn. 13 and Eqn. 14 into Eqn. 10 enables us to obtain:

$$d_i = \frac{1}{l} \left(p_2 + \frac{\int_{-\infty}^{+\infty} y_2 e^{-Ay_2^2 + By_2} dy_2}{\int_{-\infty}^{+\infty} e^{-Ay_2^2 + By_2} dy_2} \right) = \frac{1}{l} \left(p_2 + \frac{B}{2A} \right). \quad (15)$$

Finally, through simplification, Eqn. 15 can be transformed into Eqn. 4.

Before depth supervision, we normalize both the captured depth and predicted depth to 0 – 1 as follows:

$$R(D) = \begin{cases} \frac{1}{2\beta} D & (D < \beta) \\ 1 - \frac{\beta}{2D} & (D \geq \beta) \end{cases}, \quad (16)$$

where $\beta = 10$, as the depth values within 10 meters are accurate. In this way, the same depth error results in a greater loss when closer to the camera than at further distances. It effectively avoids excessive depth loss for distant Gaussians due to inherently large depth values. This normalization also facilitates the storage of depth maps.